# Deployment of an electrocorticography system with a soft robotic actuator

Sukho Song[1,2], Florian Fallegger[1], Alix Trouillet[1], Kyungjin Kim[1,3], Stéphanie P. Lacour[1]*

Electrocorticography (ECoG) is a minimally invasive approach frequently used clinically to map epileptogenic regions of the brain and facilitate lesion resection surgery and increasingly explored in brain-machine interface applications. Current devices display limitations that require trade-offs among cortical surface coverage, spatial electrode resolution, aesthetic, and risk consequences and often limit the use of the mapping technology to the operating room. In this work, we report on a scalable technique for the fabrication of large-area soft robotic electrode arrays and their deployment on the cortex through a square-centimeter burr hole using a pressure-driven actuation mechanism called eversion. The deployable system consists of up to six prefolded soft legs, and it is placed subdurally on the cortex using an aqueous pressurized solution and secured to the pedestal on the rim of the small craniotomy. Each leg contains soft, microfabricated electrodes and strain sensors for real-time deployment monitoring. In a proof-of-concept acute surgery, a soft robotic electrode array was successfully deployed on the cortex of a minipig to record sensory cortical activity. This soft robotic neurotechnology opens promising avenues for minimally invasive cortical surgery and applications related to neurological disorders such as motor and sensory deficits.

## INTRODUCTION

Electrocorticography (ECoG) grids are a class of surface electrode implants used to investigate neural activities across large areas of the brain (*1–4*). ECoG grids find a wide variety of applications in basic neuroscience and clinical settings, including brain function monitoring (*5–8*), alleviation of epileptic seizures (*9*), brain function recovery (*10, 11*), pain modulation (*12*), speech recognition (*13*), and brain-computer interfaces (*14*). The large-area coverage of ECoG grids is especially useful in investigating neurological disorders associated with several regions of the brain, such as spreading depolarizations after traumatic brain injury (*4, 15, 16*). However, challenges arise when implanting grids with large surface areas (such as >10 cm$^2$) over the cerebral cortex.

Conventional research and clinical ECoG grids are mechanically passive devices, which are surgically laid over the cortex after a craniotomy that exposes the brain (*17*). The size of the craniotomy is at least as large as the footprint of the ECoG grid (in some cases, smaller ECoG strips may be inserted below the skull). Neural recordings are usually performed intraoperatively or over short periods of time (<30 days) during which the patient remains at the hospital. A cranioplasty using autologous skull or synthetic materials completes the procedure. The large craniotomies are often a limiting factor in the use of ECoG grids, considering both the risk-benefit ratio and acceptability of the procedure by the patients. Post-surgical complications may arise, including inflammatory responses and scarring, morphological changes to the brain, and neurological deficiencies (*18–21*). An alternative to such planar ECoG grids is stereotactic electroencephalography probes that are implanted through small burr holes (<1 cm$^2$) in the skull, thereby having a lower risk profile than ECoG (*22*).

In this work, we propose a deployable ECoG system, assisted with soft robotic actuation, to surgically implant large-area and soft microfabricated ECoG grids on the cortex through small burr holes. The deployment approach relies on a bioinspired, soft robotic mechanism called eversion (*23*). The ECoG grid was prepared with a soft micromachining process that enabled thin (<400 μm thick), dura mater–like electrode implants (*24*).

Eversion is an actuation mechanism that relies on the deployment of initially inverted, structurally cylindrical thin-walled sleeves. When pressurized, the sleeves flip inside out, elongate, and move forward. Eversion has been used in a wide variety of different applications ranging from medical catheters (*25*) to friction-less rubber seals in a rolling diaphragm cylinder (*26*). The mechanism has recently been rediscovered by Hawkes and colleagues and used for a bioinspired soft robot that could "grow" longitudinally, squeeze through small openings, and explore constrained environments (*27–30*).

Here, we developed a soft robotic ECoG system using eversion actuation as a deployment mechanism for large surface areas. The system was also implemented with built-in strain sensors, which monitor, in real time, the deployment of the soft implant under the skull. The sensors provided critical feedback on when to stop the everting motion. The micromachined elastomeric sleeve with a hydrophilic inner surface allowed controlled eversion through pressurized dispensing of a biocompatible lubricant, such as saline solution. Furthermore, the entirely soft, thin-walled everting ECoG system ensured an intimate contact with the curvilinear brain surface. Last, an in vivo demonstration showed full functionalities of the proposed ECoG system through eversion, deployment sensing, and acute neural recording on a minipig model.

[1]Laboratory for Soft Bioelectronic Interfaces, Neuro-X Institute, Ecole Polytechnique Fédérale de Lausanne (EPFL), 1202 Geneva, Switzerland. [2]Laboratory of Sustainability Robotics, Swiss Federal Laboratories for Materials Science and Technology (Empa), 8600 Dübendorf, Switzerland. [3]Department of Mechanical Engineering, University of Connecticut, Storrs, CT 06269, USA.
*Corresponding author. Email: stephanie.lacour@epfl.ch

## RESULTS

### Design and fabrication of the soft ECoG system

The eversion mechanism, strain sensor, and neural electrodes were combined into a single deployable ECoG system using a soft micromachining process (Fig. 1A). Two planar elastomeric membranes made of polydimethylsiloxane (PDMS) were stacked to form the implantable interface. The inner surface of the PDMS-made implant was treated to be hydrophilic (fig. S1, C and D), enabling lubrication with biocompatible aqueous fluids. The first membrane hosted the microelectrode arrays and strain sensors (24) prepared with the silicone-on-silicon process (31) and displayed natural dura mater–like compliance. Metallic tracks (Fig. 1Biii) were thermally evaporated (35-nm-thick gold thin film) on top of the elastomer surface to form microcracked elastic interconnects that sustain stretch over 30% strain without electrical failure (24, 32). Electrode sites were coated with a platinum (Pt)–PDMS composite that established an intimate contact with the nervous tissue to support low electrical impedance and mechanical compliance (Fig. 1Bii) (33). Resistive strain sensors were prepared on the elastomeric substrate with similar microcracked gold thin film (34). The second membrane of plain silicone was bonded at the edge of the first membrane using a soluble sacrificial layer as a spacer and completed the leg-shaped tubular stack. A thin flexible printed circuit board was integrated with the interconnects to form a low geometrical profile connector. The detailed fabrication process is available in Materials and Methods and the Supplementary Materials (fig. S1).

Figure 1B shows a photograph of a soft ECoG system containing six actuated legs (6 mm wide and 0.4 mm thick) (Fig. 1Bi). Each leg contains four interconnects, associated microelectrodes (red in Fig. 1Bi) surrounded by a strain sensor patterned on the outer contour of the deployable strip (green in Fig. 1Bi). In preparation for surgical implantation, the ECoG system was secured to a loader connector using a thin layer of vinylsiloxane silicone elastomer to provide a temporary seal between the array and the loader (fig. S2). Biocompatible aqueous solution [such as saline, phosphate-buffered saline (PBS) solution, or dextran solution] was used as a lubricant to reduce layer friction inside the soft ECoG system during folding and deployment.

Next, the ECoG legs were folded into the 20-mm-diameter loader (Fig. 1, C to E) that matched typical 20-mm burr holes. The rigid loader was positioned on the cranium immediately above the preliminary drilled circular burr hole. Figure 1Ei shows the three-step deployment process within a hydrogel phantom human brain [agarose, 0.5 weight % (wt %)] and a transparent plastic (polyethylene terephthalate) skull. A positive fluidic pressure differential was applied inside the loader, increasing the fluidic force $F$ at the everting tip (Fig. 1Ci). The array stayed folded until the fluidic force overcame friction $f$ with respect to the increase in the positive fluidic pressure differential. When the fluidic force became greater than the friction, the folded array was gently pushed out of the tip via eversion by flipping inside out and extended under the stiff skull (Fig. 1Cii). As the eversion created new volume to lengthen the array from the tip, the fluidic pressure differential dropped. The tip growth stopped as the fluidic pressure became smaller than the friction and until the pressure differential increased sufficiently to reiterate the above cycle. Note that the highest-pressure differential for deployment remained constant for a given leg cross-section

($mm^2$ range) independently of its length, which is one of the main advantages of the pressure-driven eversion.

A mechanical support made of 50-μm-thick polyimide film prevented the circular PDMS diaphragm at the center of the soft ECoG system from inflating and compressing the brain by bulging out with the positive pressure differential. Figure 1Dii shows a 40-mm-diameter, fully deployed implantable system. During deployment, which typically lasted 30 to 40 s per leg (movie S1), the inflated legs could slightly push against the brain. The resultant compressive strains are discussed in the next section. Once the system was fully deployed and depressurized, the high compliance (Young's modulus, $E$, of about 700 kPa) and low profile (thickness, $h$, of about 0.4 mm) of the deployable ECoG grids allowed intimate contact with the surface of the brain with improved conformability to existing clinical ECoGs (fig. S3). After the ECoG monitoring, the deployed grids could be easily pulled out from the brain, similarly to nondeployable implants (31).

### Structural characterization of the soft ECoG system

Implementing pressure-driven eversion within the subdural cortical space calls for minimal compression of the underlying brain tissue. To do so, we first investigated the shape and geometrical parameters of deployable legs, namely, the leg width $w$ and thickness $h$ on straight single legs (Fig. 2Ai), the taper angle $a$ on tapered legs (Fig. 2Aii), and the radius of curvature $r_c$ on curved legs (Fig. 2Aiii). Deployment characterization was performed using compressed air to readily monitor the air pressure differential $P_a$ inside structural prototypes as the pressure gradually increased and then suddenly dropped at the moment of deployment. We defined the metric $P_d$, for deployment pressure, as the maximum air pressure differential to quantitatively evaluate the deployability of each design (Fig. 2B). The highest $P_d$ indicates the most difficult design to deploy. Figure 2C (i and ii) and movie S2 display the deployment of two distinct leg geometries with the tapered and curved configuration. The width and thickness, $w$ and $h$, of straight legs notably affected $P_d$ during deployment (Fig. 2Di): $P_d$ increased as the leg narrowed and thickened. In the present design, $P_d$ increased by 2.8 times regardless of the width $w$ if the thickness $h$ was doubled. On the other hand, the taper angle (curvature) minimally affected $P_d$ and the leg deployability (Fig. 2D, ii and iii). Increasing the curvature of the legs was of particular interest because larger surface coverage may be reached (Fig. 2Aiii and movie S3). $P_d$ stayed nearly constant, at 10.4 kPa on average, regardless of $r_c$ ranging from 6 to 30 mm, showing that $r_c$ did not have any substantial effects on $P_d$ (Fig. 2Diii).

Upon pressurization, each leg inflated with oval cross-sections owing to its rectangular relaxed shape. Such inflation may locally and momentarily compress the underlying brain. To quantify the resulting displacements, we measured the local strain maps in phantom brain models using a digital image correlation technique and computed them using finite element modeling (Fig. 3). The cross-sectional shape of the inflated leg evolved from oval to circular with increasing $P_d$ (fig. S4A). The circumferential elongation of the leg envelope remained negligible until the circular shape appeared with high enough $P_d$ (fig. S4A, iii and iv). Such large radial expansion was, however, not observed for legs with $h < 0.4$ mm and 4 mm $< w < 8$ mm.

To quantify eventual brain compression upon pressurization of the leg, we designed a mock system of the brain and cranium using a
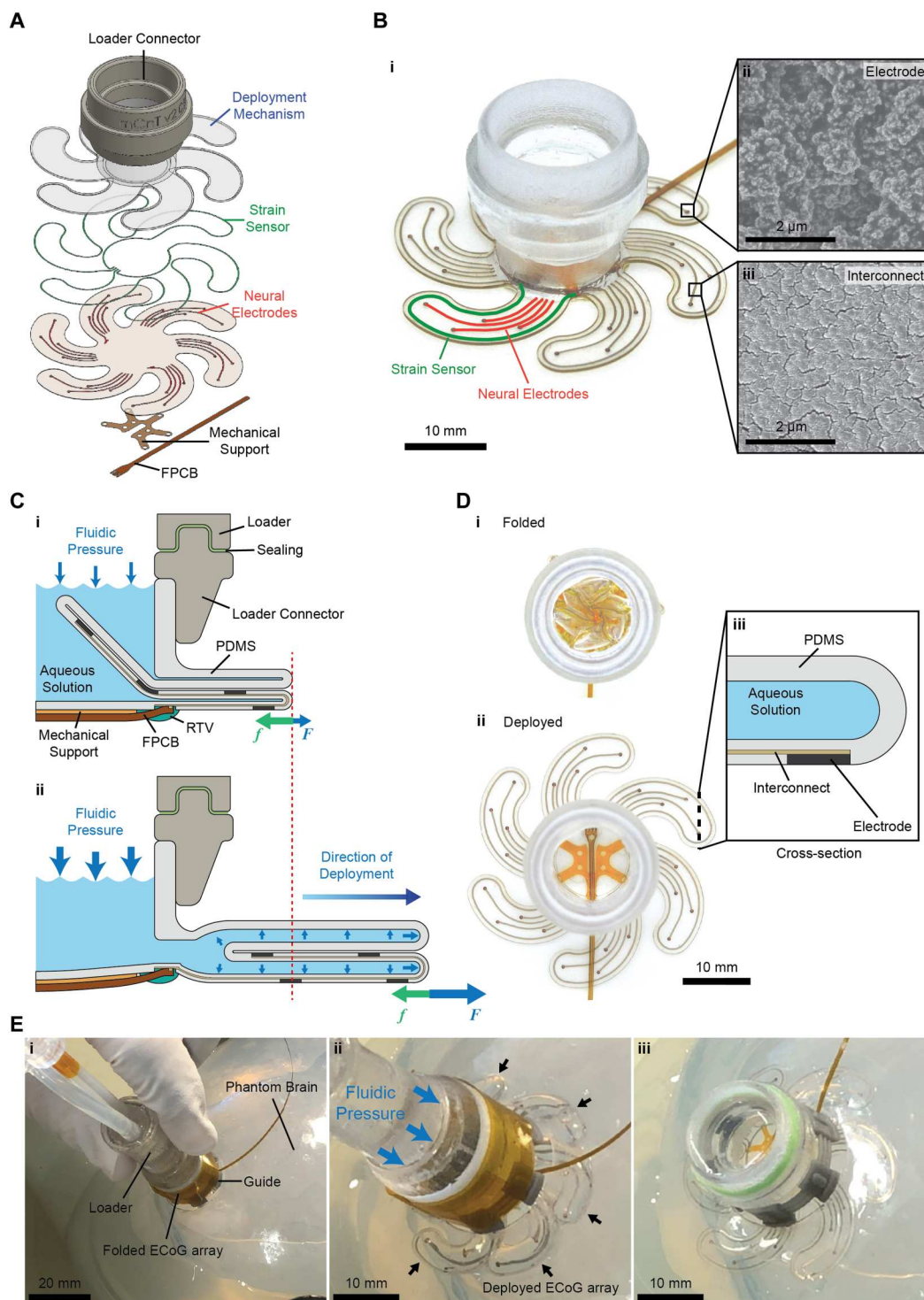
**Fig. 1. Design, fabrication, and working principle of the deployable ECoG system.** (**A**) An image of a multilegged soft ECoG array consisting of the actuation mechanism, strain sensor, and surface electrodes. (**B**) Photographic images of the ECoG array prototype: (i) an overview, (ii) a scanning electron microscope (SEM) image of Pt-PDMS composite, and (iii) an SEM image of microcracked gold thin-film interconnect. (**C**) Schematic cross-sections of the soft ECoG system: (i) folded and (ii) deployed with a positive fluidic pressure differential. The red dashed line indicates the initial position of the leg before deployment. $F$ and $f$ indicate fluidic force and friction, respectively. (**D**) Top view photographic images of the soft ECoG array prototype: (i) folded and (ii) fully deployed. (iii) Schematic cross-section of the ECoG array showing the inner chamber filled with aqueous solution. (**E**) Photographic images of the ECoG prototype being deployed in a phantom brain model: (i) positioning the system in a burr hole (22 mm in diameter) of the synthetic phantom brain consisting of a hydrogel block and a plastic skull, (ii) deploying the system with a positive fluidic pressure differential (arrows indicate deployed electrode arrays), and (iii) removing the loader to leave the deployed ECoG in position.
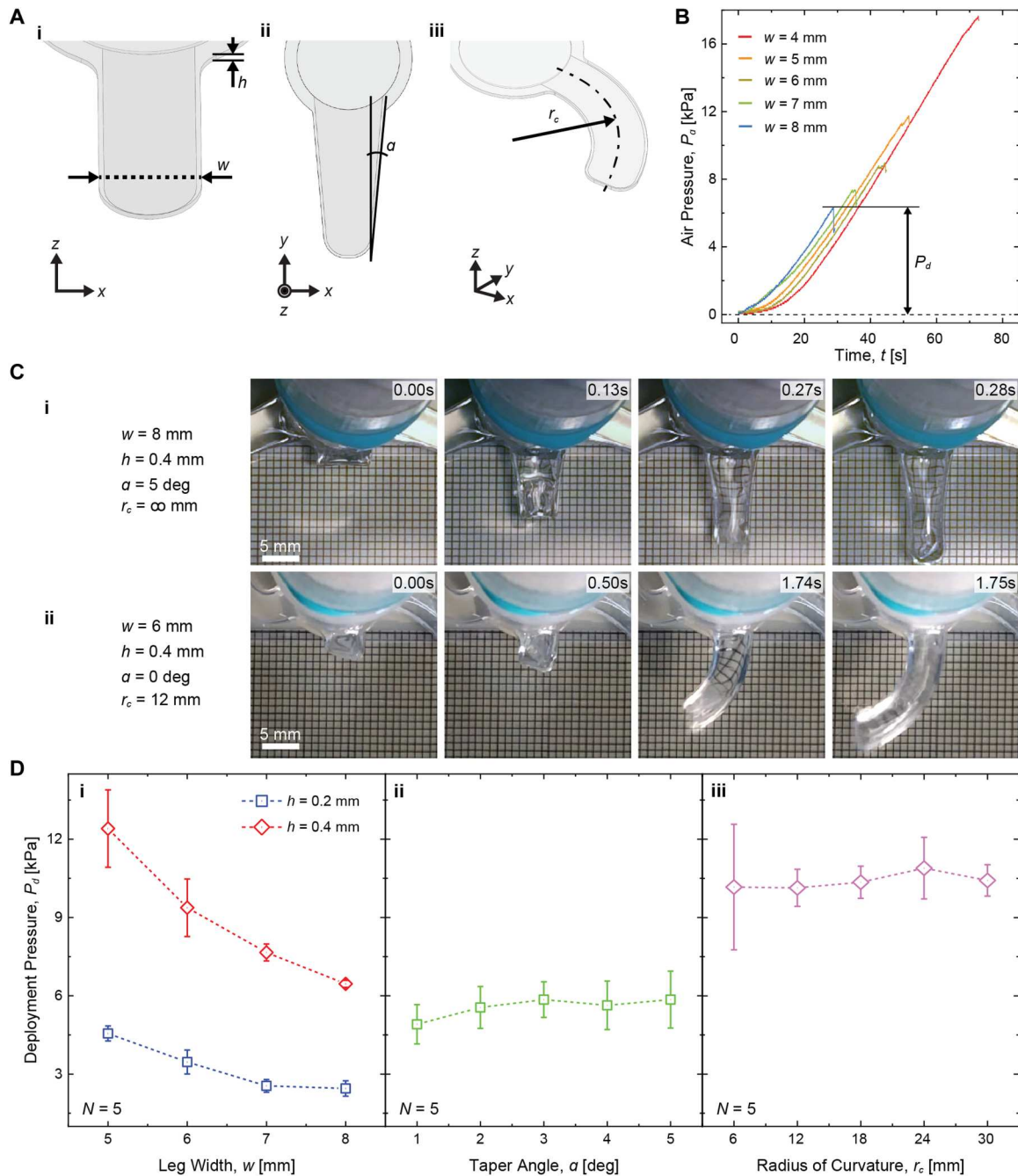
**Fig. 2. Deployability of the ECoG legs.** (**A**) Illustration of ECoG legs: (i) a straight leg with width $w$ and thickness $h$, (ii) a tapered leg with taper angle $a$, and (iii) a curved leg with radius of curvature $r_c$. (**B**) Profiles of air pressure $P_a$ inside straight legs with respect to time $t$, depending on different widths $w$. By default, $h = 0.4$ mm, $a = 0°$, and $r_c = \infty$ mm. (**C**) Sequential images of the deployment of the ECoG legs: (i) a tapered leg and (ii) a curved leg. (**D**) Deployment pressure $P_d$ depending on various design variables: (i) leg width $w$ and thickness $h$, (ii) taper angle $a$, and (iii) radius of curvature $r_c$. A statistical analysis (one-way ANOVA test) revealed that there is no statistical significance in $P_d$ with respect to a change in $a$ [$F(4, 20) = 1.01$, $P = 0.42$] and $r_c$ [$F(4, 20) = 0.27$, $P = 0.89$]. By default, $h = 0.4$ mm, $w = 6$ mm, $a = 0°$, and $r_c = \infty$ mm. Each data point in (D) is an average of five different measurements ($N = 5$) with a single specimen. Error bars indicate ±SD.

soft hydrogel brain model [agarose; 0.5 wt %, $E \sim 5.3$ kPa (*35*)] and a stiff plastic frame, respectively. The brain and skull models are 1 mm apart, accounting for the epidural space (side views in Fig. 3A). The gel was coated with randomly dispersed graphene nanoplatelets to allow for displacement tracking. A straight leg prototype ($h = 0.4$ mm and $a = 0°$) was inserted in the gap and pressurized to $P_d$

defined in Fig. 2Di (movie S4). Upon pressurization, the cross-section of the soft leg changed its shape from flat to oval, thereby compressing the hydrogel brain model (front views in Fig. 3A). The resulting density of the graphene nanoplatelets increased in the vicinity of the inflated leg (front view in Fig. 3Aii). Figure 3B displays maps of vertical displacement of the hydrogel brain
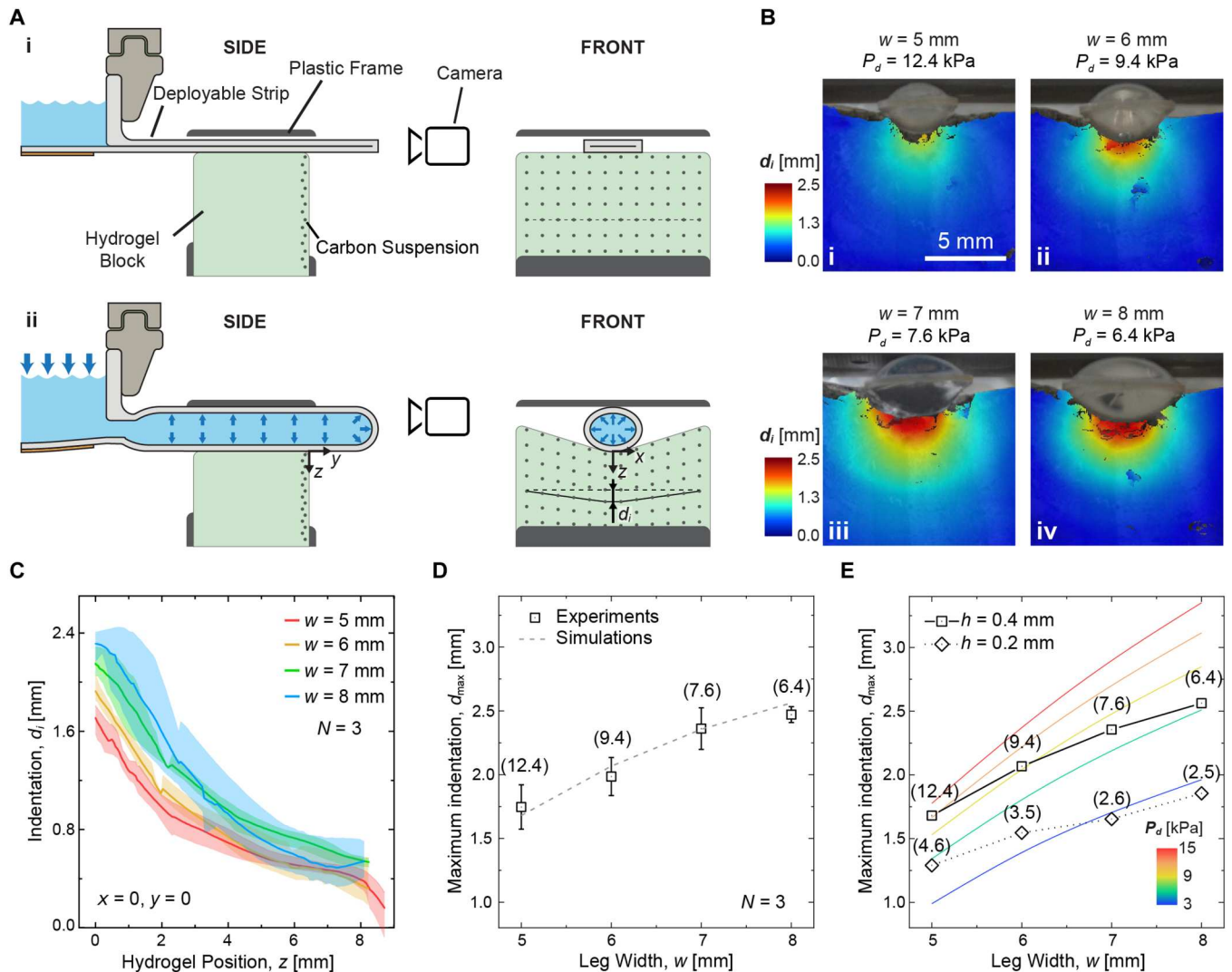
**Fig. 3. Indentation of a phantom brain depending on various deployable ECoG leg shapes.** (**A**) Schematic side view and front view of a single straight leg ($h = 0.4$ mm and $a = 0°$) with experimental setup (i) before and (ii) after pressurization. The central axis of the leg is taken as the initial reference ($x = y = z = 0$). The indentation $d_i$ is on the boundary between the bottom of the inflated leg and the hydrogel block in the final deformed configuration. Note that the actual carbon suspension is randomly dispersed on the hydrogel surface. (**B**) Color maps of $d_i$ of the hydrogel block indented by the leg with different widths: (i) $w = 5$ mm, (ii) $w = 6$ mm, (iii) $w = 7$ mm, and (iv) $w = 8$ mm. Each leg design is inflated with its corresponding $P_d$ shown in Fig. 2D (i). (**C**) Profiles of $d_i$ with respect to $z$ depending on different $w$ values. Each solid line is an average of three measurements ($N = 3$) using the same leg sample. Shaded areas show a range of the minimum and the maximum $d_i$. (**D**) Maximum indentation $d_{max}$ of various leg shapes with different widths when inflated with the corresponding $P_d$. Each data point is an average of three different measurements ($N = 3$) using the same leg sample. Error bars indicate ±SD. Dashed line represents data from calculations of the FEM model. (**E**) Numerical estimation of $d_{max}$ of various leg shapes with different $w$, $h$, and $P_d$ values. The dashed line and colored solid lines are $d_{max}$ for the leg with $h = 0.4$ mm and $h = 0.2$ mm, respectively. Numbers in the brackets in (D) and (E) are the corresponding $P_d$ values for the given $w$ and $h$.

model computed from the tracked displacement of the carbon suspension (*36*). The resulting indentation $d_i$ on the surface of the brain model was defined as the vertical displacement of the graphene nanoplatelets referenced to their initial configuration (solid and dashed lines, respectively, in front views in Fig. 3A, i and ii). The center of the coordinate system (or the origin) of the indentation map was defined at the bottom center of the inflated leg as shown in Fig. 3 (Aii and B).

Figure 3C displays $d_i$ along the $z$ axis ($x = y = 0$) as a function of the hydrogel depth $z$ for different leg widths (5 mm < $w$ < 8 mm). The gel displacement $d_i$ was maximal $d_i = d_{max}$ immediately below

the central axis of the leg ($x = y = z = 0$) and plateaued at about 0.6 mm at a depth of about 6 mm, independent of the leg width. Wider legs induced larger overall displacement of the underlying gel ($d_{max}$ = 1.7 to 2.5 mm for $w = 5$ to 8 mm wide, respectively), although its slope became smaller with the increase in leg width as predicted by the finite element models (FEMs) (Fig. 3D). This may be explained as wider legs being able to deploy with a smaller $P_d$, thereby inducing lower compression on the brain phantom. The experiments and simulations were in good agreement (Fig. 3D), with an overall deviation of only 0.06 mm from the average of the measured $d_{max}$.

With the verified model, we estimated the effect of reduction in device thickness on the indentation of the cortex. We numerically calculated $d_{max}$ of leg strips with half the thickness ($h = 0.2$ mm) compared with the experimentally tested legs ($h = 0.4$ mm). The 0.2-mm-thick leg strip in the FEM was inflated virtually with its corresponding $P_d$ measured in Fig. 2Di (Fig. 3E). $d_{max}$ for the 0.2-mm-thick leg strip (dotted line) showed about 0.6 mm less indentation on average than $d_{max}$ for the 0.4-mm-thick leg strip (dashed line). This decrease in $d_{max}$ was attributed to the prompt eversion associated with 2.8 times smaller $P_d$ for the thinner legs. Note that this FEM computes $d_{max}$ on the basis of $P_d$ when the implantable system is deployed in an unconstrained environment. The computed $d_{max}$ values are therefore underestimated. This is because of factors, such as poor lubrication, a reduced gap between the brain and the skull, adhesion between the skull and the dura mater in case of epidural implantation, or high curvature of the skull, that can increase $P_d$ (see the effects of the increased $P_d$ on $d_{max}$ as shown by the colored solid lines in Fig. 3E).

### Proof of concept of the soft ECoG system in vivo

Next, we investigated the potential of the deployable ECoG system in vivo to record cortical brain activity acutely in a minipig model. Geometrical features of the minipig's brain (such as curvature of the brain) are close to that of the human brain (37). Design considerations were made to limit the indentation on the cortex to as small as 2 mm. This dimension proved to be a safe limit in human brain surgeries (38). The system also needs to be deployed with minimal fluidic pressure to permit slow and less invasive eversion. We developed an implantable soft ECoG prototype with a straight single leg with 6-mm width, 0.4-mm thickness, and 15-mm length that satisfies the above design criteria. The estimated indentation depth was about 2 mm based on the data in Fig. 3 with the lowest deployment pressure among possible design options. The 15-mm leg strip was long enough to target the rostrum somatosensory cortex when deployed from the top of the brain.

Photographs of the folded (preimplantation) and deployed soft ECoG are shown in Fig. 4A. The deployable system supports a three-by-four electrode array (0.3-mm diameter, 1.5-mm center-to-center pitch) with metallic interconnects and a strain sensor (Fig. 4Aiii) that are made of microcracked gold thin film (Fig. 1Biii) (24). The strain sensor surrounded the array and allowed real-time monitoring of the status of the leg deployment. First, the implant was folded within the holder using a small plastic rod (movie S5). Here, ethanol lubricated the contact surface between the ECoG leg strip and the plastic rod. The lubricant evaporated quickly from the leg surface and disappeared shortly after the plastic rod was removed before the in vivo use. The initial resistance $R_o$ of the strain sensor (in its flat form) was about 10 kilohms and increased up to several megohms upon folding (Fig. 4B). The resistance after folding $R_f$ remained in the megohm range during deployment with an increasing $P_a$ and recovered its initial low value once the array laid flat (Fig. 4C, $R_d < 15$ kilohms at $t > 27$ s; movie S5). Although there were two orders of magnitude difference in electrical track resistance between $R_f$ and $R_d$, the resistance after deployment $R_d$ remained constant after 50 cycles of repetitive folding and deployment (Fig. 4D), indicating that the microcracked gold film sustained such demanding mechanical loading. Figure 4E shows that folding and deployment also had minimal effect on electrochemical impedance of the electrode sites, confirming their robustness to extreme deformations.

Instead of using compressed air, deployment could also be induced by incompressible fluid medium (15 wt % dextran in this case), which resulted in slower deployment speed (Fig. 4F). The incompressible aqueous solution filling the entire deployment system prevented buildup of the pneumatic energy compared with the compressed air, which led to fast and uncontrolled deployment (fig. S5 and movie S6).

### In vivo validation of the soft ECoG system

We demonstrated the in vivo deployment and recording capability of the soft ECoG system via eversion in an anesthetized Göttingen minipig model. The model has a large gyrencephalic brain with a vascular density and skull thickness similar to those of humans (39). We recorded somatosensory evoked potentials (SSEPs) at the surface of the brain in response to the electrical stimulation of the snout. A single-legged, straight ECoG strip (Fig. 4A) was deployed subdurally at the surface of the cortex targeting the frontal lobe and the somatosensory region. The dimensions of the soft implant supported a deployment from the superior part of the skull and thus did not require a craniotomy above the central sinus vein or displacement of the temporal muscle laterally.

The deployable ECoG system was first filled from the inside with PBS and was folded using a plastic rod with ethanol as shown in movie S5. After complete ethanol evaporation, the folded array was thoroughly rinsed again with PBS to make sure that there was no ethanol residue in contact with the brain. After durotomy (Fig. 5Ai; see Materials and Methods for details), the loader was placed at the surface of the brain. The base of the device was placed in contact with the cortex, at the frontal edge of the craniotomy with the folded leg facing the anterior section (Fig. 5Aii). A syringe pump was used to inject PBS into the loader to initiate and control the subdural deployment. The strain sensor output indicated when the soft leg was fully deployed ($R_d = 21$ kilohms at $t = 42$ s; Fig. 5B). Next, the loader was removed, and the implant was electrically connected to the electrophysiology recording system.

We recorded evoked potentials from the somatosensory cortex induced by electrical stimulation of the snout delivered at three distinct locations of the snout and two stimulation amplitudes (Fig. 5Ci). Averaged signals from selected channels presented depolarization and polarization peaks (Fig. 5C, ii and iii) and a timing similar to that of a previous report for SSEPs (40). The SSEPs with amplitudes reaching >30-$\mu$V peak amplitudes displayed location-specific characteristics of amplitude and waveform that were consistent with a spatial map of the snout representation (41). The position of the deployed array on the somatosensory area was confirmed postmortem (Fig. 5D) (37). The soft implant did not present any folded part and conformed well with the cortical surface (Fig. 5E, i to iii). No visible damage was evident under or in the vicinity of the deployment location after whole-brain extraction. In particular, morphological change or ruptured tissues due to the deployment of the everting strip were not visible (Fig. 5Eiv and fig. S6). Postmortem histochemistry was also performed to further analyze inflammation and neuronal health. Coronal sections were stained using three markers—Iba1, GFAP, and NeuN—for microglial cells, astrocytes, and neurons, respectively, at three different locations under the implanted zone corresponding to base, stem, and tip of the deployed ECoG (fig. S7A). Cross-sectional images confirmed that there was no visible damage outside and under the implanted zone and no indentation of the brain, suggesting that the eversion-based
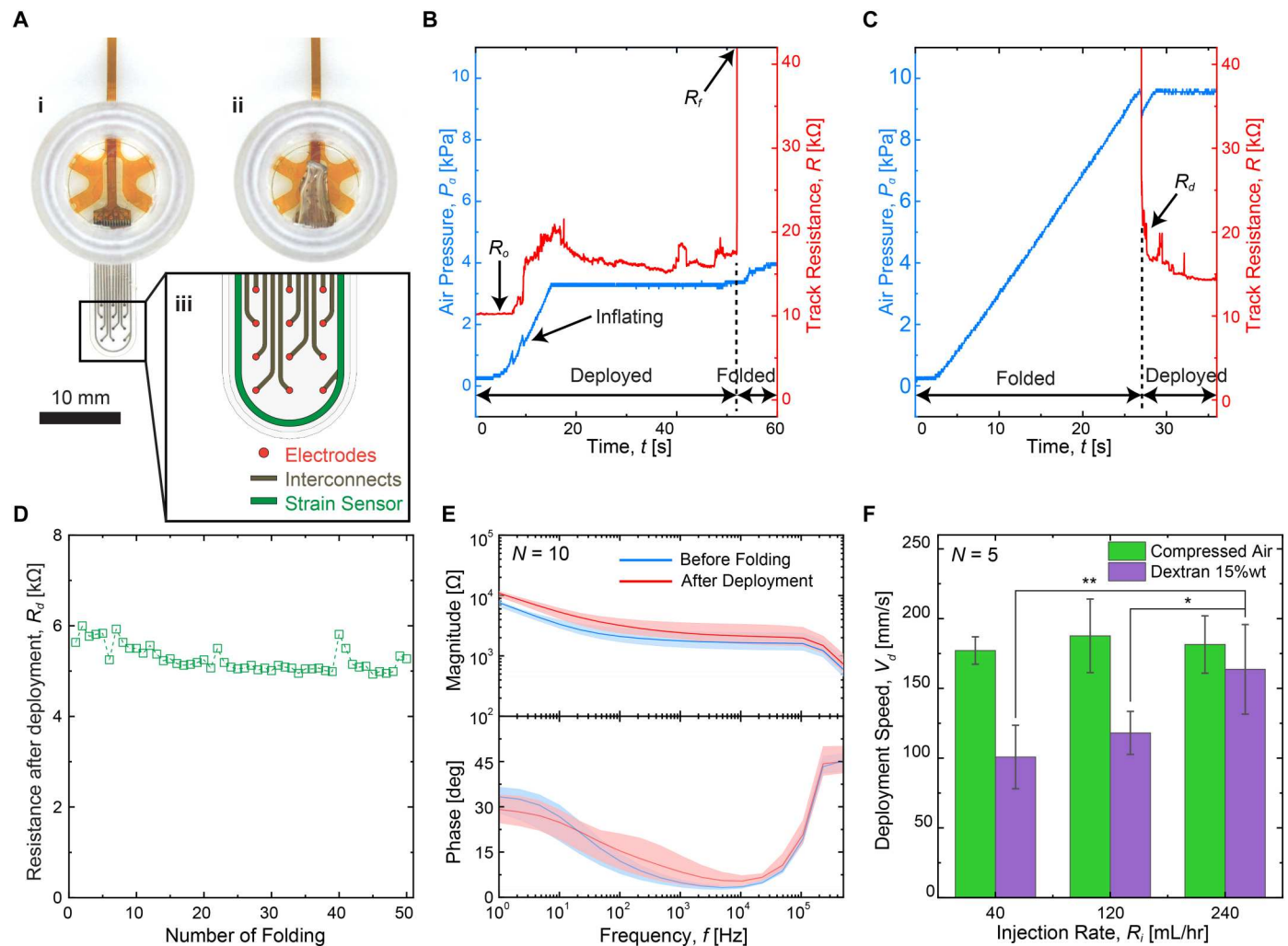
**Fig. 4. Functional verification of the soft ECoG system.** (**A**) Photographs of the top view of a soft ECoG array (single straight leg prototype): (i) deployed and (ii) folded. (iii) Layout of the electrodes, interconnects, and strain sensor. (**B**) Profiles of internal air pressure $P_a$ and track resistance $R$ of strain sensor with respect to time $t$ during folding and (**C**) deployment. $R_o$, $R_f$, and $R_d$ indicate the initial track resistance before folding, track resistance after folding, and track resistance after deployment, respectively. (**D**) Track resistance after deployment $R_d$ with respect to the number of folding. (**E**) Electrochemical impedance magnitude (top) and phase (bottom) of 10 channels ($N = 10$) on the functional soft ECoG array before folding (blue) and after deployment (red) as a function of frequency. Shaded areas show a range of the minimum and the maximum phase and magnitude. (**F**) Deployment speed $V_d$ of the deployable strip filled with different fluids as a function of injection rate $R_i$. Each data point is an average of five different measurements ($N = 5$) using the same strip sample. Error bars indicate ±SD. A statistical analysis (one-way ANOVA test) revealed that there is no statistical significance in $V_d$ depending on $R_i$ for the compressed air [$F(2, 12) = 0.35$, $P = 0.71$], unlike the case of aqueous solution (15 wt % dextran) [$F(2, 12) = 8.87$, $P = 0.004$]. *$P < 0.05$ and **$P < 0.01$.

deployment was soft and gentle to the brain tissue as designed (fig. S7, B and F). At the microscopic level, sporadic microglial activation was noticed in the vicinity of the base and the stem (zones i and ii, fig. S7E, i and ii) but not in the tip (zone iii, fig. S7Eiii). No notable glial cell reaction (fig. S7E) or limited astrocyte proliferation was observed (fig. S7C). In addition, neuron imaging showed intact cortical layers (fig. S7D), except for the stem that displayed some loss of neurons on a limited part under the implanted zone (fig. S7Bii). Note that no glial cell activation, astrocyte proliferation, or neuronal loss was observed in the tip where the cortical tissue sustains lower compression than that at the implant base (lower form factor of the implant rounded tip). Although multiple factors (such as indentation depth and deployment speed) can contribute to the damage

mentioned above, this result suggests that minor modifications to the current design, such as thinner or narrower legs, may be sufficient to ensure the safety of the implanted brain at a microscopic level. These are initial observations from an acute test ($N = 1$) that will need consolidation across a larger number of animals and longer time points.

## DISCUSSION

Conventional ECoG grids are mechanically passive devices and are used clinically in conjunction with extensive craniotomies that typically expose the cortex over areas at least as large as the size of the neural interface. Various adverse effects can be associated with large
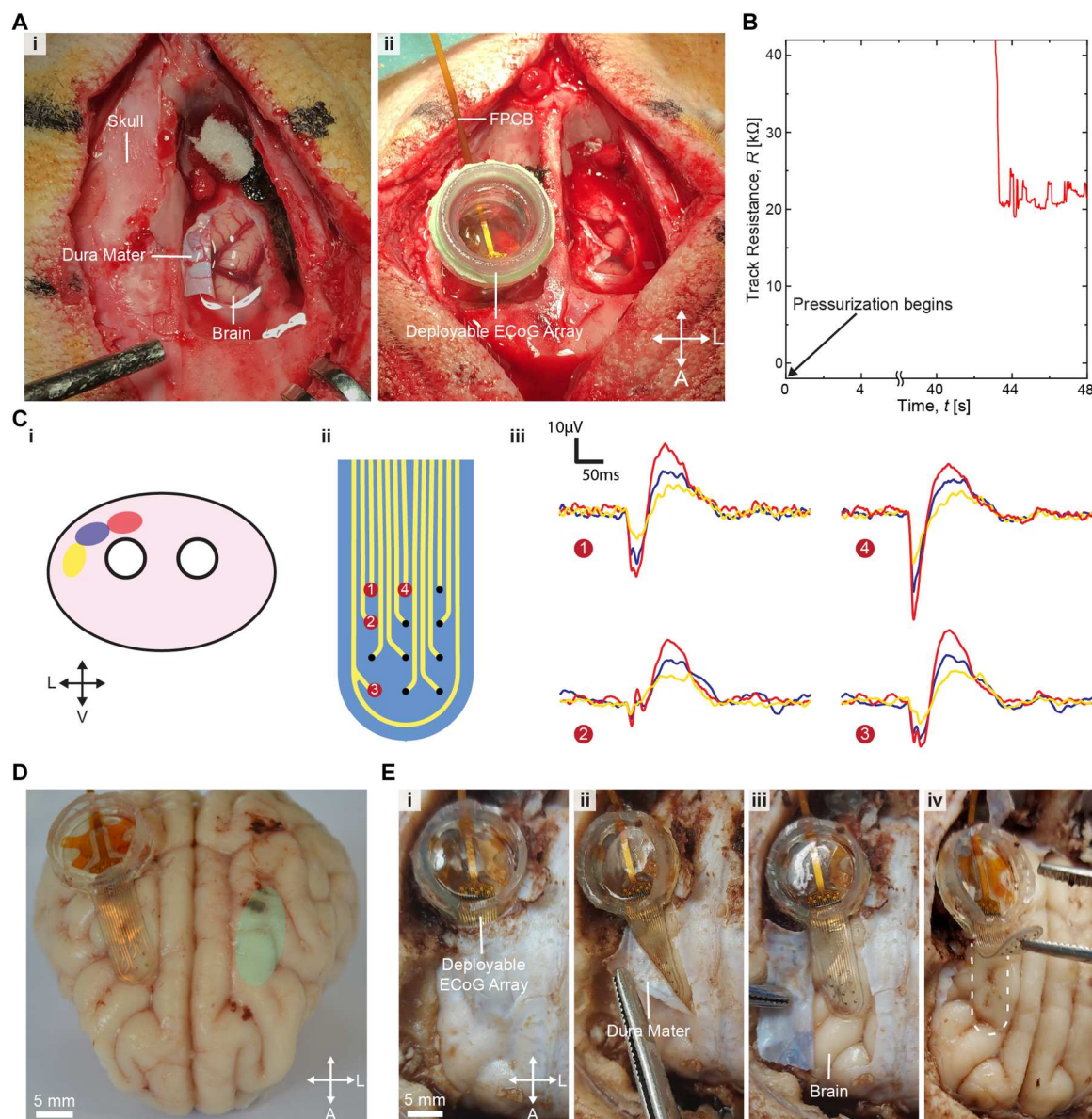
**Fig. 5. In vivo acute recording of SSEPs in a minipig model.** (**A**) Surgical access for the deployment of the soft robotic ECoG array on the brain: (i) overview of the access to the brain and (ii) ECoG system after placement on the brain. (**B**) Changes in the electrical track resistance of the strain sensor during the deployment procedure. (**C**) Recording of the SSEPs on the brain after deployment of the ECoG array: (i) location of the three placements of stimulation on the snout, (ii) electrode design, and (iii) SSEPs from the snout stimulation according to the snout stimulation position [color codes match with (i)]. (**D**) Photograph of the extracted brain with the position of the electrode array depicted in green on the contralateral hemisphere. (**E**) Extraction of the ECoG array after the brain perfusion showing the deployed soft array. The dashed line in (iv) overlaps with the area initially covered by the deployed ECoG strip.

craniotomies, including high risk of infection, possible brain damage, and aesthetic impairments of remaining large scars (20). These risks substantially limit the adoption of ECoG arrays for large-scale functional brain mapping or permanent cortical implants for brain-machine interfaces.

To mitigate these effects, minimally invasive deployment methods for ECoG arrays have been recently explored. Thin implants can be steered and positioned on the rat cortex using a pair of magnets across the skull (with one external magnet and another one embedded in the implant) (42). However, the translation to the human skull, which is eight times thicker than that of rodents, is challenging (43, 44). Woodington et al. (45) leveraged microfluidic actuation to unfold a thin, rolled electrode paddle at the surface of the spinal cord of a human cadaver. The unfurling actuation required preinsertion of a rolled-up paddle on the brain or on the spinal cord before deployment, which may result in greater preinsertion depth and a larger craniotomy proportional to the array size.

The brain is the softest organ of the body (46, 47), and insertion into its structure may lead to catastrophic consequences for neuronal network activity and overall brain function. Robotic deployment of the soft ECoG in the epidural space—a constrained gap between the skull and the cortex—should be highly controlled. Periodic

variations in arterial blood pressure during cardiac cycle and respiration are accompanied by constant motion of the brain (*48*), which further calls for soft, biomimetic designs that do not trigger adverse immune responses and tissue damage (*49–51*).

In this work, we leveraged soft robotics and soft bioelectronic devices to propose an implantable system that answers clinical needs related to safety, cortex coverage, and electrophysiologic sensing. The fluid-based eversion can produce sufficient actuation force to deploy the implant in the subdural space. The eversion-based ECoG system retained the folded strips outside the skull and maintained a low thickness profile during deployment on the final surface area of the implant, which provided a critical advantage over other deployment mechanisms for large electrode areas. The folded strips were fed from a loader situated outside the skull through a burr hole. Therefore, a larger surface area of the deployed electrodes requires only a bigger loader without increasing the size of craniotomy or the compression depth on the brain (fig. S8). Furthermore, the everting ECoG system was entirely developed from a soft and biocompatible elastomer with Young's modulus less than 1 MPa, which is comparable to that of the biological dura mater (*24*).

An important consideration in the design of the deployable ECoG is its insertion and deployment over the largest possible surface area. Hawkes *et al.* (*29*) demonstrated that eversion has no limit on the length of deployable strip through a given hole size. This implies that the eversion-based deployment system could ideally cover the entire cortex area using a large size loader through a tiny burr hole suitable for just a single curved strip (fig. S8B). However, trade-offs between the deployment pressure, geometry, and electrode density are needed before applying the above scenario to a practical application. For example, reducing the number of legs requires increasing the integration density markedly [such as the connection pitch to electrically connect the metallic interconnect to the flexible printed circuit board (FPCB) cable]. Therefore, the multilegged configuration in Fig. 1B should be chosen over the single curved leg design presented in fig. S8B if the number of electrodes on the implant increases. In addition, the deployment pressure can be substantially reduced by reducing the thickness of the soft substrate (Fig. 2Di), which will lead to a smaller indentation of the brain during implantation. Other design strategies, such as increasing the number of strips while reducing leg width or incorporating variable leg curvature along the leg length, also need to be considered before reaching the final implant design (fig. S9). Overall, further advances in thin-film manufacturing and packaging technology in conjunction with the shape optimization discussed above will enable improved soft robotic ECoG arrays for human neurosurgeries (*52*) with higher area coverages and larger safety margins than the devices shown in this work as a proof of concept.

Proprioception, the perception of position and movement of the body, is a critical and important concept for a robotic device but has not been demonstrated by previous deployment systems for neural implants. The proposed soft ECoG system includes a built-in sensor informing in real time on the status of deployment. This is enabled through thin metallic film strain sensors that are integrated within the implantable system. The use of resistance change for conductive elastomer composites or liquid metals has prevailed as strain sensors for the purpose of touch or motion sensing of various wearable and soft robotic devices (*53–57*). Here, we leveraged the strain sensitivity of thin gold film for in situ and real-time deployment detection. Inversion or full eversion of the deployable ECoG strip led to a substantial change in the track resistance of the microcracked gold strain sensor, which nevertheless displayed reproducible performance for up to 50 reversible loading cycles (Fig. 4D). Unlike medical imaging tools (such as fluoroscopy) requiring manual intervention from a human surgeon for controlled deployment, the strain sensor can easily be incorporated into a closed-loop feedback control system to precisely manipulate a pressure source to increase, decrease, or stop the pressurization of the deployable ECoG system automatically.

We have shown that by combining soft robotic actuation, proprioceptive sensing, and soft bioelectronic neurotechnology, we can engineer an implantable soft robotic neural interface for minimally invasive implantation of large-area electrode arrays with a customized electrode layout. In vivo acute brain recording of minipig SSEPs demonstrated typical local field potentials with amplitudes and timings comparable to those of previous reports (*40*). No visible morphological damage could be observed after implantation (Fig. 5). However, local microscopic damage shown in the histochemistry analysis (fig. S7) calls for further optimization toward biosafety of the deployment system. Future work replicating these initial findings will further assess the surgical procedure as well as the design and suitability of the deployable system as a chronic neurotechnology. Usability also needs to be optimized for adoption in a surgical setting, such as improvements in the securing and removal of the loader connector. Further advances in soft electrode manufacturing should be made to miniaturize the soft ECoG array and to enable multilegged and curved deployment systems with high area coverages.

The concept of combining soft robotics and soft bioelectronics can present more applications beyond neurotechnology (*58–62*) because the leg and electrodes can be adapted for specific geometrical constraints and targeted organs. For example, deployment over the heart may allow the epicardial mapping of the electrical activity for the diagnosis of atrial fibrillation with much more coverage and precision than current catheter-based solutions (*63*). Moreover, the ability to deploy a large electrode array through a small opening may be leveraged in laparoscopic surgeries for mapping bowel, renal, or liver electrical activity (*64, 65*). Furthermore, spinal cord stimulation electrode arrays (*45, 66*) may be inserted using a single leg design while minimizing the size of spinal cord exposure, which is not possible with conventional open surgery or dual laminectomy (*24*). The proposed soft robotic neural interface opens promising avenues for the development of accessible and minimally invasive surface implants for patients. Improved safety and usability of the soft CoG system may find a wide range of possible applications for the treatment of various neurological disorders.

## MATERIALS AND METHODS
### Study design
The main objective of this study was to combine soft robotic sensing, an actuation mechanism called eversion, and implantable soft microelectrode arrays for minimally invasive ECoG. Experiments in this study were designed to characterize the effect of various design parameters on the system performance and to validate the proposed functionalities of the implant as follows. The deployment pressure was measured five times ($N = 5$) for each deployable ECoG strip design corresponding to a different combination of design parameters in leg width, thickness, taper angle, and

radius of curvature. The indentation of the hydrogel blocks was measured three times ($N = 3$) for each straight ECoG strip ($h = 0.4$ mm) with four different leg widths ($w = 5, 6, 7$, and $8$ mm). The electrical track resistance of the strain sensor was measured by folding and unfolding a single-legged ECoG array 50 times. The electrochemical impedance spectroscopy of electrode sites and gold interconnects was performed on 10 working electrode sites ($N = 10$). Last, the measurements of deployment speed were performed five times ($N = 5$) on a straight ECoG strip ($h = 0.4$ mm, $a = 6$ mm, and $w = 6$ mm) filled with two different fluid medium conditions at three different syringe pump speeds (40, 120, and 240 ml/hour). All experiments were performed more than three times ($N > 3$) to estimate mean value and SD of each measurement. Also, there was no specific treatment of outliers, and all measured data were included. Detailed information about measurement techniques can be found in the Supplementary Materials.

### Fabrication and experimental setup

Both functional and structural samples of deployable ECoG systems were made of medical-grade PDMS elastomer (LSR M130, Elkem Silicones) based on the silicone-on-silicon process established in our previous work. Samples prepared for structural characterization were fabricated without the interconnects and Pt-PDMS electrode coatings. According to our experiments, PBS (pH 7.4; Gibco) washes out the dextran coating inside the deployable ECoG strip deposited in the process (fig. S1E) over multiple foldings and deployments. The PDMS surface inside the deployable ECoG tube changed from hydrophilic to hydrophobic, which meant it could not be lubricated with the aqueous solution anymore. Therefore, those structural samples were filled with 15 wt % dextran solution serving as a lubricant for long-term and repetitive eversion. In the case of the functional deployable ECoG strip equipped with electrodes and interconnects for in vivo testing, on the other hand, the sample was filled with PBS to achieve the maximum biocompatibility with the brain tissue for a few instances of eversion within a short period. Please see the "Fabrication methods" and "Experimental methods" sections in the Supplementary Materials for a complete description.

### In vivo acute neural recording

Surgical procedures were approved by the local ethical committee in accordance with the guidelines for the Care and Use of Laboratory Animals and approved by local (Canton of Geneva) and federal (Swiss) veterinary authorities with authorization number GE11120A. The single-legged deployable soft robotic ECoG array shown in Fig. 4Ai was used for the in vivo experiment. A Göttingen minipig of 8.5 kg (3 months old) was anesthetized with a premedication mix of azaperone (0.4 mg/kg), midazolam (0.75 mg/kg), and atropine (0.2 mg/ml) and induced with 6% sevoflurane. After intubation, an intravenous line was placed on the ear for continuous administration of propofol (10 ml/hour) at 2 wt % and along a bolus of fentanyl (2 µg/kg) during the heavy surgical procedures. The surgery was performed as follows: A large frontal-to-posterior incision was made over the midline. The muscle was retracted, and the periosteum was removed using an elevator. The midline and bregma were identified. The craniotomy was planned 2 mm laterally from the midline to 20 mm and −10 mm to +20 mm anterior to frontal. The skull was drilled with a neurosurgery drill (B. Braun ELAN 4 using a 2.5-mm neuro cutter drill bit) until reaching the

dura. Then, the boneflap was broken free using a spatula. The dura mater was incised with a microscalpel (stab scalpel knife, Fine Science Tools) in a U shape away from the midline. The dura mater was placed toward the midline and kept hydrated. The loader system with the soft robotic ECoG array, filled with 15% dextran, was placed at the frontal edge of the craniotomy and kept in place using a bench stand. The soft robotic ECoG array was deployed using the linear syringe pump, and electrical resistance of the strain sensor was monitored with the microcontroller using the customized LABVIEW code. After the deployment, the sensory evoked potentials were elicited using bipolar needles inserted in the snout (2 mm inside the skin) and stimulated with an isolated pulse generator (isolated pulse generator model 2100, AM Systems) at 5 and 10 mA, symmetric, cathodic-first, biphasic pulses with a 300-µs pulse width at a 2-Hz repetition rate. The brain signals were acquired by connecting the FPCB on the implant to a custom-printed circuit board connected to a wireless head stage amplifier system (Multichannel Systems Wireless W2100). A ground wire was inserted epidurally on the contralateral side. The acquisition was performed at a sampling frequency of 2 kHz with a digital Butterworth bandpass filter of 1 to 200 Hz and a notch filter at 50 Hz. The recorded signals were averaged over each individual stimulation pulse for a total of 30 s (roughly 60 epochs per condition). The experiment was performed for different stimulation pulse amplitudes (baseline, 5 and 10 mA) for the three snout stimulation positions. After the recordings, two catheters were inserted in the right jugular aorta vein, and the animal was sacrificed using 5 ml of pentobarbital injected intravenously. Then, 1 liter of 0.1 M PBS with heparin (100,000 U for 1 liter) was injected at 200 ml/min using a peristaltic pump (Shenchen LabS3/UD15) followed by 5 liters of a PBS solution containing 4% paraformaldehyde (PFA) at 200 ml/min. After the perfusion, the animal was decapitated using a scalpel knife to incise the skin and muscle between the first and second vertebrae. The head was then postfixed in 4% PFA solution for a few days. The brain with the deployed soft robotic ECoG array was then extracted by removing first the skin and muscle using a scalpel knife and then the bone using bone rongeurs. The dura mater was carefully incised to reveal the deployment status of the implant. Last, after removal of the device, the whole brain was extracted from the skull cavity.

### Postmortem histochemistry

The explanted brain was postfixed in 4% PFA solution for 48 hours before the hemispheres were separated using a scalpel knife. Then, parallel cuts were made at the front and back of the implantation area to isolate a block for further sectioning. The block was immersed in 15 wt % and then 30 wt % sucrose solution for 3 days each. The brain block was then frozen in isopentane at −55°C in a tissue-freezing system (Excilone Snapfrost). The frozen brain was then sliced in 40-µm sections using a cryostat (Leica CM1950). Immunostaining was then performed on several sections covering the entire zone of implantation. After incubation in 0.3% Triton and 3% bovine serum albumin, tissues were incubated with primary antibodies for 48 hours at room temperature (Anti-GFAP, Rat, Thermo Fisher Scientific, #13-0300; Anti-Iba1, Rabbit, Fuji-Film, 019-19741; Anti-NeuN, GuineaPig, Sigma-Aldrich, ABN90) followed by secondary antibody incubation for 2 hours at room temperature (Alexa Fluor 488, Thermo Fisher Scientific, #A-11006; Alexa Fluor 647, Thermo Fisher Scientific, #A-21245;

Alexa Fluor 555, Thermo Fisher Scientific, #A-21435). After mounting, slides were imaged at ×10 magnification using a Slide Scanner microscope (Olympus VS120).

## Statistical analysis

Mean and SD were used for statistical analysis in quantifying the effect of different design variables on the system performance, whereas the minimum and the maximum were used as a shaded area in visualizing the range of system response to a given input (such as compression on the brain in Fig. 3C or electrical impedance in Fig. 4E). One-way analysis of variance (ANOVA) with post hoc Tukey's honestly significant difference test was performed using Origin 2022 (OriginLab Corp.) when estimating a statistical significance depending on more than two groups of a parameter. The statistical significance was determined using $P$ values, and a value higher than 0.05 ($P > 0.05$) was considered statistically significant (*$P < 0.05$ and **$P < 0.01$). The ANOVA results were reported in figure legends using the following format "$F(dfB, dfW) = F$-statistic, $P = P$ value", where dfB and dfW are degrees of freedom between groups and degrees of freedom within groups, respectively.

## Supplementary Materials

**This PDF file includes:**
Fabrication methods
Experimental methods
Figs. S1 to S12
Table S1
Reference (67)

**Other Supplementary Material for this manuscript includes the following:**
Movies S1 to S6
MDAR Reproducibility Checklist

## REFERENCES AND NOTES

1. A. Palmini, The concept of the epileptogenic zone: A modern look at Penfield and Jasper's views on the role of interictal spikes. *Epileptic Disord.* **8**, 10–15 (2006).
2. J. P. Mullin, D. Sexton, S. Al-Omar, W. Bingaman, J. Gonzalez-Martinez, Outcomes of subdural grid electrode monitoring in the stereoelectroencephalography Era. *World Neurosurg.* **89**, 255–258 (2016).
3. P. C. D. W. Hamer, S. G. Robles, A. H. Zwinderman, H. Duffau, M. S. Berger, Impact of intraoperative stimulation brain mapping on glioma surgery outcome: A meta-analysis. *J. Clin. Oncol.* **30**, 2559–2565 (2012).
4. J. A. Hartings, C. Li, J. M. Hinzman, C. W. Shuttleworth, G. L. Ernst, J. P. Dreier, J. A. Wilson, N. Andaluz, B. Foreman, A. P. Carlson, Direct current electrocorticography for clinical neuromonitoring of spreading depolarizations. *J. Cereb. Blood Flow Metab.* **37**, 1857–1870 (2017).
5. D. De Ridder, G. De Mulder, T. Menovsky, S. Sunaert, S. Kovacs, Electrical stimulation of auditory and somatosensory cortices for treatment of tinnitus and pain. *Prog. Brain Res.* **166**, 377–388 (2007).
6. M. Lauritzen, J. P. Dreier, M. Fabricius, J. A. Hartings, R. Graf, A. J. Strong, Clinical relevance of cortical spreading depression in neurological disorders: Migraine, malignant stroke, subarachnoid and intracranial hemorrhage, and traumatic brain injury. *J. Cereb. Blood Flow Metab.* **31**, 17–35 (2011).
7. R. P. Lesser, N. E. Crone, W. R. S. Webber, Subdural electrodes. *Clin. Neurophysiol.* **121**, 1376–1392 (2010).
8. J. C. Bulacio, L. Jehi, C. Wong, J. Gonzalez-Martinez, P. Kotagal, D. Nair, I. Najm, W. Bingaman, Long-term seizure outcome after resective surgery in patients evaluated with intracranial electrodes. *Epilepsia* **53**, 1722–1730 (2012).
9. G. Nune, S. Arcot Desai, B. Razavi, M. A. Agostini, G. K. Bergey, A. A. Herekar, L. J. Hirsch, R. W. Lee, P. A. Rutecki, S. Srinivasan, P. C. van Ness, T. K. Tcheng, M. J. Morrell, Treatment of drug-resistant epilepsy in patients with periventricular nodular heterotopia using RNS® system:
Efficacy and description of chronic electrophysiological recordings. *Clin. Neurophysiol.* **130**, 1196–1207 (2019).
10. M. J. Vansteensel, E. G. M. Pels, M. G. Bleichner, M. P. Branco, T. Denison, Z. V. Freudenburg, P. Gosselaar, S. Leinders, T. H. Ottens, M. A. van den Boom, P. C. van Rijen, E. J. Aarnoutse, N. F. Ramsey, Fully implanted brain–computer interface in a locked-in patient with ALS. *N. Engl. J. Med.* **375**, 2060–2066 (2016).
11. W. Wang, J. L. Collinger, A. D. Degenhart, E. C. Tyler-Kabara, A. B. Schwartz, D. W. Moran, D. J. Weber, B. Wodlinger, R. K. Vinjamuri, R. C. Ashmore, J. W. Kelly, M. L. Boninger, An electrocorticographic brain interface in an individual with tetraplegia. *PLOS ONE* **8**, e55344 (2013).
12. J.-J. Mo, W. H. Hu, C. Zhang, X. Wang, C. Liu, B. T. Zhao, J. J. Zhou, K. Zhang, Motor cortex stimulation: A systematic literature-based analysis of effectiveness and case series experience. *BMC Neurol.* **19**, 48 (2019).
13. J. G. Makin, D. A. Moses, E. F. Chang, Machine translation of cortical activity to text with an encoder–decoder framework. *Nat. Neurosci.* **23**, 575–582 (2020).
14. P. D. Marasco, J. S. Hebert, J. W. Sensinger, D. T. Beckler, Z. C. Thumser, A. W. Shehata, H. E. Williams, K. R. Wilson, Neurorobotic fusion of prosthetic touch, kinesthesia, and movement in bionic upper limbs promotes intrinsic brain behaviors. *Robotics* **6**, eabf3368 (2021).
15. D. Y. Chung, F. Oka, C. Ayata, Spreading depolarizations: A therapeutic target against delayed cerebral ischemia after subarachnoid hemorrhage. *J. Clin. Neurophysiol.* **33**, 196–202 (2016).
16. J. A. Hartings, M. R. Bullock, D. O. Okonkwo, L. S. Murray, G. D. Murray, M. Fabricius, A. I. Maas, J. Woitzik, O. Sakowitz, B. Mathern, B. Roozenbeek, H. Lingsma, J. P. Dreier, A. M. Puccio, L. A. Shutter, C. Pahl, A. J. Strong; Co-Operative Study on Brain Injury Depolarisations, Spreading depolarisations and outcome after traumatic brain injury: A prospective observational study. *Lancet Neurol.* **10**, 1058–1064 (2011).
17. T. Kaiju, K. Doi, M. Yokota, K. Watanabe, M. Inoue, H. Ando, K. Takahashi, F. Yoshida, M. Hirata, T. Suzuki, High spatiotemporal resolution ECoG recording of somatosensory evoked potentials with flexible micro-electrode arrays. *Front. Neural Circuits* **11**, 20 (2017).
18. M. J. Mack, Minimally invasive and robotic surgery. *JAMA* **285**, 568–572 (2001).
19. S. R. Dashti, H. Baharvahdat, R. F. Spetzler, E. Sauvageau, S. W. Chang, M. F. Stiefel, M. S. Park, N. C. Bambakidis, Operative intracranial infection following craniotomy. *Neurosurg. Focus* **24**, E10 (2008).
20. J. T. Cole, A. Yarnell, W. S. Kean, E. Gold, B. Lewis, M. Ren, D. C. McMullen, D. M. Jacobowitz, H. B. Pollard, J. T. O'Neill, N. E. Grunberg, C. L. Dalgard, J. A. Frank, W. D. Watson, Craniotomy: True sham for traumatic brain injury, or a sham of a sham? *J. Neurotrauma* **28**, 359–369 (2011).
21. C. Lin, X. Zhao, H. Sun, Analysis on the risk factors of intracranial infection secondary to traumatic brain injury. *Chin. J. Traumatol.* **18**, 81–83 (2015).
22. J. Parvizi, S. Kastner, Promises and limitations of human intracranial electroencephalography. *Nat. Neurosci.* **21**, 474–483 (2018).
23. J. D. Greer, T. K. Morimoto, A. M. Okamura, E. W. Hawkes, A. Soft, A soft, steerable continuum robot that grows via tip extension. *Soft Robot.* **6**, 95–108 (2019).
24. I. R. Minev, P. Musienko, A. Hirsch, Q. Barraud, N. Wenger, E. M. Moraud, J. Gandar, M. Capogrosso, T. Milekovic, L. Asboth, R. F. Torres, N. Vachicouras, Q. Liu, N. Pavlova, S. Duis, A. Larmagnac, J. Vörös, S. Micera, Z. Suo, G. Courtine, S. P. Lacour, Electronic dura mater for long-term multimodal neural interfaces. *Science* **347**, 159–163 (2015).
25. I. W. Scudamore, B. C. Dunphy, I. D. Cooke, Outpatient falloposcopy; intra-luminal imaging of the fallopian tube by trans-uterine fibre-optic endoscopy as an outpatient procedure. *BJOG* **99**, 829–835 (1992).
26. J. Hepp, A. Badri-Spröwitz, A novel spider-inspired rotary-rolling diaphragm actuator with linear torque characteristic and high mechanical efficiency. *Soft Robot.* **9**, 364–375 (2022).
27. N. D. Naclerio, A. Karsai, M. Murray-Cooper, Y. Ozkan-Aydin, E. Aydin, D. I. Goldman, E. W. Hawkes, Controlling subterranean forces enables a fast, steerable, burrowing soft robot. *Robotics* **6**, eabe2922 (2021).
28. J. Luong, P. Glick, A. C. Ong, M. S. deVries, S. Sandin, E. Hawkes, M. Tolley, Eversion and retraction of a soft robot towards the exploration of coral reefs, in *2019 2nd IEEE International Conference on Soft Robotics (RoboSoft)* (IEEE, 2019), pp. 801–807.
29. E. W. Hawkes, L. H. Blumenschein, J. D. Greer, A. M. Okamura, A soft robot that navigates its environment through growth. *Robotics* **2**, eaan3028 (2017).
30. N. D. Naclerio, C. M. Hubicki, Y. O. Aydin, D. I. Goldman, E. W. Hawkes, Soft robotic burrowing device with tip-extension and granular fluidization, in *2018 IEEE/RSJ International Conference on Intelligent Robots and Systems (IROS)* (IEEE, 2018), pp. 5918–5923.
31. G. Schiavone, F. Fallegger, X. Kang, B. Barra, N. Vachicouras, E. Roussinova, I. Furfaro, S. Jiguet, I. Seáñez, S. Borgognon, A. Rowald, Q. Li, C. Qin, E. Bézard, J. Bloch, G. Courtine, M. Capogrosso, S. P. Lacour, Soft, implantable bioelectronic interfaces for translational research. *Adv. Mater.* **32**, 1906512 (2020).
32. S. P. Lacour, D. Chan, S. Wagner, T. Li, Z. Suo, Mechanisms of reversible stretchability of thin metal films on elastomeric substrates. *Appl. Phys. Lett.* **88**, 204103 (2006).

33. I. R. Minev, N. Wenger, G. Courtine, S. P. Lacour, Research update: Platinum-elastomer mesocomposite as neural electrode coating. *APL Mater.* **3**, 014701 (2015).

34. H. O. Michaud, J. Teixidor, S. P. Lacour, Soft metal constructs for large strain sensor membrane. *Smart Mater. Struct.* **24**, 035020 (2015).

35. V. Normand, D. L. Lootens, E. Amici, K. P. Plucknett, P. Aymard, New insight into agarose gel mechanical properties. *Biomacromolecules* **1**, 730–738 (2000).

36. J. Blaber, B. Adair, A. Antoniou, Ncorr: Open-source 2d digital image correlation matlab software. *Exp. Mech.* **55**, 1105–1122 (2015).

37. P. Sauleau, E. Lapouble, D. Val-Laillet, C. H. Malbert, The pig model in brain imaging and neurosurgery. *Animal* **3**, 1138–1151 (2009).

38. F. Meinert, P. Dömer, S. O. A. Helgers, L. Schumm, N. Hecht, J. P. Dreier, J. Woitzik, Subdural placement of electrocorticographic electrode array through a burr hole exposure: 2-dimensional operative video. *Oper. Neurosurg.* **23**, e169 (2022).

39. M. M. Swindle, A. Makin, A. J. Herron, F. J. Clubb Jr., K. S. Frazier, Swine as models in biomedical research and toxicology testing. *Vet. Pathol.* **49**, 344–356 (2011).

40. M. Gierthmuehlen, T. Ball, C. Henle, X. Wang, J. Rickert, M. Raab, T. Freiman, T. Stieglitz, J. Kaminsky, Evaluation of μECoG electrode arrays in the minipig: Experimental procedure and neurosurgical approach. *J. Neurosci. Methods* **202**, 77–86 (2011).

41. F. Fallegger, G. Schiavone, E. Pirondini, F. B. Wagner, N. Vachicouras, L. Serex, G. Zegarek, A. May, P. Constantin, M. Palma, M. Khoshnevis, D. van Roost, B. Yvert, G. Courtine, K. Schaller, J. Bloch, S. P. Lacour, MRI-compatible and conformal electrocorticography grids for translational research. *Adv. Sci.* **8**, 2003761 (2021).

42. U.-J. Jeong, J. Lee, N. Chou, K. Kim, H. Shin, U. Chae, H. Y. Yu, I. J. Cho, A minimally invasive flexible electrode array for simultaneous recording of ECoG signals from multiple brain regions. *Lab Chip* **21**, 2383–2397 (2021).

43. M. A. O'Reilly, A. Muller, K. Hynynen, Ultrasound insertion loss of rat parietal bone appears to be proportional to animal mass at submegahertz frequencies. *Ultrasound Med. Biol.* **37**, 1930–1937 (2011).

44. E. M. Lillie, J. E. Urban, S. K. Lynch, A. A. Weaver, J. D. Stitzel, Evaluation of skull cortical thickness changes with age and sex from computed tomography scans. *J. Bone Miner. Res.* **31**, 299–307 (2016).

45. B. J. Woodington, V. F. Curto, Y. L. Yu, H. Martínez-Domínguez, L. Coles, G. G. Malliaras, C. M. Proctor, D. G. Barone, Electronics with shape actuation for minimally invasive spinal cord stimulation. *Advances* **7**, eabg7833 (2021).

46. Z. Li, H. Yang, G. Wang, X. Han, S. Zhang, Compressive properties and constitutive modeling of different regions of 8-week-old pediatric porcine brain under large strain and wide strain rates. *J. Mech. Behav. Biomed. Mater.* **89**, 122–131 (2019).

47. S. Budday, T. C. Ovaert, G. A. Holzapfel, P. Steinmann, E. Kuhl, Fifty shades of brain: A review on the mechanical testing and modeling of brain tissue. *Arch. Comput. Methods Eng.* **27**, 1187–1230 (2020).

48. I. Terem, W. W. Ni, M. Goubran, M. S. Rahimi, G. Zaharchuk, K. W. Yeom, M. E. Moseley, M. Kurt, S. J. Holdsworth, Revealing sub-voxel motions of brain tissue using phase-based amplified MRI (aMRI). *Magn. Reson. Med.* **80**, 2549–2559 (2018).

49. S. Wurth, M. Capogrosso, S. Raspopovic, J. Gandar, G. Federici, N. Kinany, A. Cutrone, A. Piersigilli, N. Pavlova, R. Guiet, G. Taverni, J. Rigosa, P. Shkorbatova, X. Navarro, Q. Barraud, G. Courtine, S. Micera, Long-term usability and bio-integration of polyimide-based intraneural stimulating electrodes. *Biomaterials* **122**, 114–129 (2017).

50. A. D. Degenhart, J. Eles, R. Dum, J. L. Mischel, I. Smalianchuk, B. Endler, R. C. Ashmore, E. C. Tyler-Kabara, N. G. Hatsopoulos, W. Wang, A. P. Batista, X. T. Cui, Histological evaluation of a chronically-implanted electrocorticographic electrode grid in a non-human primate. *J. Neural Eng.* **13**, 046019 (2016).

51. A. Lecomte, E. Descamps, C. Bergaud, A review on mechanical considerations for chronically-implanted neural probes. *J. Neural Eng.* **15**, 031001 (2018).

52. S. Emich, M. Dollenz, Burr hole is not burr hole: Technical considerations to the evacuation of chronic subdural hematomas. *Acta Neurochir.* **157**, 497–499 (2015).

53. L. Dejace, H. Chen, I. Furfaro, G. Schiavone, S. P. Lacour, Microscale liquid metal conductors for stretchable and transparent electronics. *Adv. Mater. Technol.* **6**, 2100690 (2021).

54. Y.-L. Park, B.-R. Chen, R. J. Wood, Design and fabrication of soft artificial skin using embedded microchannels and liquid conductors. *IEEE Sensors J.* **12**, 2711–2718 (2012).

55. M. A. Robertson, L. Dejace, S. P. Lacour, J. Paik, Bi-modal control of vacuum-powered soft pneumatic actuators with embedded liquid metal-based strain sensitive skin, in *2019 2nd IEEE International Conference on Soft Robotics (RoboSoft)* (IEEE, 2019), pp. 217–221.

56. L. Dejace, N. Laubeuf, I. Furfaro, S. P. Lacour, Gallium-based thin films for wearable human motion sensors. *Adv. Intell. Syst.* **1**, 1900079 (2019).

57. A. P. Gerratt, H. O. Michaud, S. P. Lacour, Elastomeric electronic skin for prosthetic tactile sensation. *Adv. Funct. Mater.* **25**, 2287–2295 (2015).

58. J. Viventi, D. H. Kim, L. Vigeland, E. S. Frechette, J. A. Blanco, Y. S. Kim, A. E. Avrin, V. R. Tiruvadi, S. W. Hwang, A. C. Vanleer, D. F. Wulsin, K. Davis, C. E. Gelber, L. Palmer, J. van der Spiegel, J. Wu, J. Xiao, Y. Huang, D. Contreras, J. A. Rogers, B. Litt, Flexible, foldable, actively multiplexed, high-density electrode array for mapping brain activity in vivo. *Nat. Neurosci.* **14**, 1599–1605 (2011).

59. F. Fallegger, G. Schiavone, S. P. Lacour, Conformable hybrid systems for implantable bioelectronic interfaces. *Adv. Mater.* **32**, 1903904 (2020).

60. L. Xu, S. R. Gutbrod, A. P. Bonifas, Y. Su, M. S. Sulkin, N. Lu, H. J. Chung, K. I. Jang, Z. Liu, M. Ying, C. Lu, R. C. Webb, J. S. Kim, J. I. Laughner, H. Cheng, Y. Liu, A. Ameen, J. W. Jeong, G. T. Kim, Y. Huang, I. R. Efimov, J. A. Rogers, 3D multifunctional integumentary membranes for spatiotemporal cardiac measurements and stimulation across the entire epicardium. *Nat. Commun.* **5**, 3329 (2014).

61. D.-H. Kim, J. Viventi, J. J. Amsden, J. Xiao, L. Vigeland, Y. S. Kim, J. A. Blanco, B. Panilaitis, E. S. Frechette, D. Contreras, D. L. Kaplan, F. G. Omenetto, Y. Huang, K. C. Hwang, M. R. Zakin, B. Litt, J. A. Rogers, Dissolvable films of silk fibroin for ultrathin conformal bio-integrated electronics. *Nat. Mater.* **9**, 511–517 (2010).

62. C. M. Tringides, N. Vachicouras, I. de Lázaro, H. Wang, A. Trouillet, B. R. Seo, A. Elosegui-Artola, F. Fallegger, Y. Shin, C. Casiraghi, K. Kostarelos, S. P. Lacour, D. J. Mooney, Viscoelastic surface electrode arrays to interface with viscoelastic tissues. *Nat. Nanotechnol.* **16**, 1019–1029 (2021).

63. C. P. Teuwen, C. Kik, P. Knops, Quantification of the arrhythmogenic effects of spontaneous atrial extrasystole using high-resolution epicardial mapping. *Circ. Arrhythm. Electrophysiol.* **11**, e005745 (2018).

64. A. Farajidavar, Bioelectronics for mapping gut activity. *Brain Res.* **1693**, 169–173 (2018).

65. L. Miller, A. Farajidavar, A. Vegesna, Use of bioelectronics in the gastrointestinal tract. *Cold Spring Harb. Perspect. Med.* **9**, a034165 (2019).

66. M. Capogrosso, T. Milekovic, D. Borton, F. Wagner, E. M. Moraud, J. B. Mignardot, N. Buse, J. Gandar, Q. Barraud, D. Xing, E. Rey, S. Duis, Y. Jianzhong, W. K. D. Ko, Q. Li, P. Detemple, T. Denison, S. Micera, E. Bezard, J. Bloch, G. Courtine, A brain–spine interface alleviating gait deficits after spinal cord injury in primates. *Nature* **539**, 284–288 (2016).

67. T. Trantidou, Y. Elani, E. Parsons, O. Ces, Hydrophilic surface modification of PDMS for droplet microfluidics using a simple, quick, and robust method via PVA deposition. *Microsyst. Nanoeng.* **3**, 16091 (2017).

# Science Robotics

## Deployment of an electrocorticography system with a soft robotic actuator

Sukho Song, Florian Fallegger, Alix Trouillet, Kyungjin Kim, and Stphanie P. Lacour

**View the article online**
https://www.science.org/doi/10.1126/scirobotics.add1002
**Permissions**
https://www.science.org/help/reprints-and-permissions

Use of this article is subject to the Terms of service